International Journal of Thermofluids 27 (2025) 101251

Contents lists available at ScienceDirect

International Journal of Thermofluids

journal homepage: www.sciencedirect.com/journal/international-journal-of-thermofluids

Mathematical modeling of an electrified methane steam reforming unit for maritime sector decarbonization via MCFC

Stefano Moriggi [a], Daniela De Cata [b,c], Dario Bove [a,*], Barbara Bosio [a]

[a] Department of Civil, Chemical and Environmental Engineering (DICCA), University of Genoa, Via Opera Pia 15, Genoa 16145, Italy

[b] Faculty of Science and Technology for Sustainable Development and One Health, Unit of Chemical-physics Fundamentals in Chemical Engineering, Università Campus Bio-Medico di Roma, Via Alvaro del Portillo, 21, Rome 00128, Italy

[c] ENEA, Department of Energy Technologies and Renewable Sources, Laboratory for Hydrogen and new Energy Vectors (TERIN-DEC-H2V), Casaccia Research Center, via Anguillarese 301, Rome 00123, Italy

ARTICLE INFO

Keywords:
Electrified steam methane reforming
Hydrogen
MCFC
Decarbonization
Mathematical modeling

ABSTRACT

To address the global climate crisis, international initiatives such as the Conferences of Parties (COP) have promoted reducing greenhouse gas emissions. Among the sectors with the greatest impact on achieving carbon neutrality, the maritime sector faces increasing regulatory pressure to reach decarbonization. In this context, Molten Carbonate Fuel Cells (MCFCs) offer a promising solution by simultaneously generating electricity and capturing CO_2 from exhaust gases. This research aims to enhance the integration of electrified Steam Methane Reforming (eSMR) with MCFC systems for sustainable maritime applications. In fact, to sustain this process, a continuous hydrogen supply is required. This study explores an innovative "shell and tube" configuration of an eSMR as a compact and energy-efficient solution. Through simulations modeling, key parameters such as gas inlet temperature, coil temperature, and reactor geometry were analyzed to optimize reactor performance. The reactor showed excellent performance in almost all cases examined, reaching equilibrium in the first half of the reactor length. Analysis of the pitch distance showed that the radial diffusion of the reactants towards the catalyst surface seems to be the limiting phenomenon. On the other hand, the performance was found to be little affected by the gas temperature, since the catalyst is in intimate contact with the heating zone, the reactants reaching the reactive zone immediately achieve the temperature of the catalyst, which promotes its kinetics.

1. Introduction

In the context of the global climate crisis, coordinated efforts such as the Conferences of Parties (COP) have promoted international dialogue. Regarding the European Union, the primary goal, as stated in the European Green Deal, is a reduction in Greenhouse Gas (GHG) emissions of 50% by 2030 and of 100% by 2050, in order to achieve carbon neutrality [1,2]. Over the years, the regulatory framework has increasingly expanded to cover the majority of economic sectors. In particular, the energy sector remains one of the most critical due to its significant emissions from burning fossil fuels for electricity and heat supply. This has driven a strong push toward the adoption of renewable energy sources. Consequently, the industrial sector now operates under stringent guidelines aimed at curbing emissions from industrial processes and enhancing energy efficiency. Similarly, the maritime sector, responsible for 3% to 4% of global emissions [3], has recently become one of the latest sectors to be subject to regulations. Specifically, the "broader EU ETS reform" of June 2023 requires the maritime sector to comply with the trading system as of January 1, 2024 [3].

To achieve the reduction of CO_2 emissions in the maritime sector, a variety of solutions may be involved, depending on the type of ship, engine and fuel. Among the most extensively studied post-combustion treatments, this work focuses on the Molten Carbonate Fuel Cell (MCFC) technology [4–6]. This system can efficiently generate electrical energy from a compact unit while simultaneously capturing CO_2 from the exhaust gases of the ship's engines [7]. Specifically, CO_2 is recovered alongside steam, from which it can be easily separated. After water condensation, CO_2 is normally liquefied with a purity up to 99.5% [8–10]. To make this approach feasible, a continuous supply of hydrogen is required to fuel the anode side of the stack, while the cathode is supplied with the stocked CO_2-rich exhaust gas. The focus of this study is the selection of an appropriate hydrogen production

---

* Corresponding author.
E-mail address: dario.bove@unige.it (D. Bove).

https://doi.org/10.1016/j.ijft.2025.101251

method, with particular emphasis on compact and sustainable units, while also considering the need for a small footprint and low CO_2 emissions. A promising solution in this sense is represented by the electrified Steam Methane Reforming (eSMR). In eSMR the conventional burners are replaced by electrical heaters, allowing for space saving and a reduction in fossil fuel consumption for heat generation. This enables accurate thermal control and improved energy efficiency, delivering heat directly to the target process [11,12]. Among the multiple types of electrified heating systems, resistive reformers show a higher degree of maturity and research potential, as they offer flexibility to propose innovative and compact designs due to their simple working principle [12–14].

The aim of this work is the investigation and optimization of an innovative resistive eSMR configuration integrated into the MCFC process. Specifically, operating parameters such as gas inlet temperature, coil temperature, and outer radius variations were examined to optimize reactor performance through modeling simulation.

2. Mathematical model

2.1. Reactor geometry and general assumptions

The reactor geometry under investigation is similar to a shell-and-tube heat exchanger. The tubes are electrical resistances which provide heat through the coil for the strongly endothermic reaction of SMR. Each coil is coated with a thin washcoat layer of porous Al_2O_3 with Ni impregnation as active element for the catalysis. On the shell side, the gas flows in the axially, diffuses radially into the heated catalyst layer, and reacts. In the model, a single tube module is considered.

It is important to note that the outer radius of a module, R_{out}, does not represent a physical wall between the tubes but rather serves as a fictitious boundary for the modeled control volume. It represents the spacing between adjacent modules, as illustrated in Fig. 1. Beyond this distance, the gas is assumed to flow into another module, where radial diffusion is no longer considered. Consequently, the geometry of a single reacting element can be approximated as a tube-in-tube or annular configuration, with the following sections:

- $0 < r < R_{coil}$: heating resistive element
- $R_{coil} < r < R_{int}$: catalyst porous solid layer
- $R_{int} < r < R_{out}$: shell side of the gas

The different layers for a module are shown in Fig. 2. The distance between the centers of two modules is referred to as Pitch. Common assumptions for the system include a laminar flow regime, justified by the low Reynolds number of all the cases studied, and the steady-state operation of the reactor.

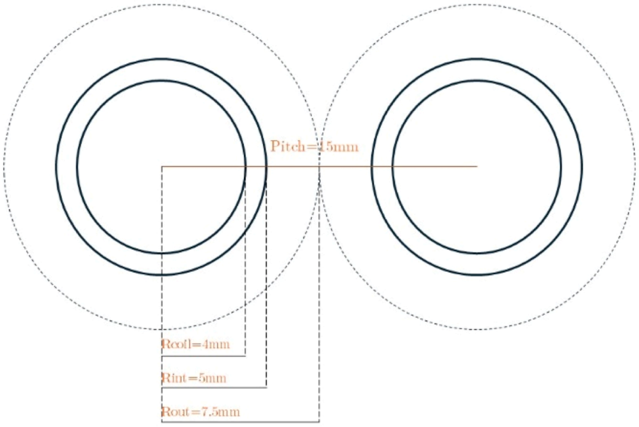

Fig. 1. Cross section of two adjacent modules.

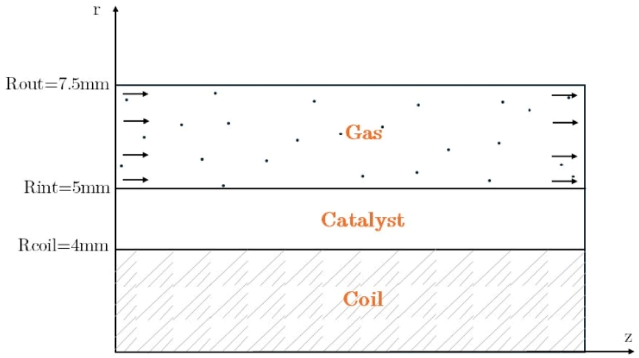

Fig. 2. Longitudinal section of a single module.

The objective of this work is to determine the optimal set of geometric parameters (e.g., tube pitch and outer radius) and operating conditions (e.g., temperature and feed concentration) to meet the requirements of the MCFC process. This is achieved by simulating a single module, whose results can be extended to any number necessary to provide an overall assessment of the reactor performance.

2.2. Kinetic model

The selected catalyst is the conventional Ni on $\alpha-Al_2O_3$, which is the most widespread for this process on an industrial scale due to its high activity, high durability and cost-effectiveness [12,15]. The kinetic model selected for this study is the widely used one proposed by Xu and Froment [16], which consists of three rate laws: steam methane reforming (SMR, Eq. 1), global reforming reaction (GRR, Eq. 2) and water-gas shift (WGS, Eq. 3).

$$CH_4 + H_2O \leftrightarrow 3H_2 + CO \tag{1}$$

$$CH_4 + 2H_2O \leftrightarrow 4H_2 + CO_2 \tag{2}$$

$$CO + H_2O \leftrightarrow H_2 + CO_2 \tag{3}$$

The respective kinetic rate can be observed in Eqs 4,5 and 6

$$r_{SMR} = \frac{k_{SMR}}{p_{H_2}^{2.5}}\left(p_{CH_4}p_{H_2O} - \frac{p_{H_2}^3 p_{CO}}{K_{p,SMR}}\right)\frac{1}{DEN^2} \tag{4}$$

$$r_{GRR} = \frac{k_{GRR}}{p_{H_2}^{3.5}}\left(p_{CH_4}p_{H_2O}^2 - \frac{p_{H_2}^4 p_{CO_2}}{K_{p,GRR}}\right)\frac{1}{DEN^2} \tag{5}$$

$$r_{WGS} = \frac{k_{WGS}}{p_{H_2}}\left(p_{CO}p_{H_2O} - \frac{p_{H_2} p_{CO_2}}{K_{p,WGS}}\right)\frac{1}{DEN^2} \tag{6}$$

When DEN^2 is a parameter that considers the adsorption equilibrium of each species into the catalyst pores [16] (see Eq. 7).

$$DEN^2 = 1 + K_{ads,CO}p_{CO} + K_{ads,H_2}p_{H_2} + K_{ads,CH_4}p_{CH_4} + K_{ads,H_2O}\frac{p_{H_2O}}{p_{H_2}} \tag{7}$$

The kinetic constants k_j and adsorption constants $K_{ads,i}$ calculated as in Eq. 8 and 9:

$$k_j = k_{j,T_r} exp\left[-\frac{E_j}{R_{gas}}\left(\frac{1}{T} - \frac{1}{T_r}\right)\right] \; j = SMR,\; GRR,\; WGS \tag{8}$$

$$K_{ads,i} = K_{ads,i,T_r} exp\left[-\frac{\Delta H_{ads,i}}{R_{gas}}\left(\frac{1}{T} - \frac{1}{T_r}\right)\right] \; i = CH_4,\; CO,\; H_2,\; H_2O \tag{9}$$

The equilibrium constants $K_{p,i}$ for SMR and WGS, they have been calculated as in [17] with the following eq. (10)

$$K_{p,i} = exp\left(\gamma_{1,i}T^{-3} + \gamma_{2,i}T^{-2} + \gamma_{3,i}T^{-1} + \gamma_{4,i}\right) \; i = SMR,\; WGS \tag{10}$$

Finally, the equilibrium constant for the GRR reaction is expressed by Eq. 11

$$K_{p,GRR} = K_{p,SMR}\ K_{p,WGS} \tag{11}$$

The kinetic parameters of the reaction model are shown in Table 1

2.3. Mass balance in the gas phase

Starting from the general form of the mass balance Eq. 12:

$$\frac{\partial C_i}{\partial t} = -\nabla\cdot N_i + g_i \tag{12}$$

The initial assumptions are the following:

- Steady state conditions
- No reactions occur in the gas phase
- Laminar flow
- Predominance of the advective term in the axial direction, due to the slim geometry considered, and therefore the high value of the Peclet number
- Diffusive flux in the radial direction

Under these hypotheses, the balance becomes (Eq. 13)

$$0 = -\nabla\cdot\left(C_i\bar{v}_z - D_{i,m}\frac{\partial C_i}{\partial r}\hat{r}\right) \tag{13}$$

Therefore, the molar balance of the i-th species in cylindrical coordinates and with plug-flow motion is given in Eq. 14.

$$\frac{\partial C_i}{\partial z} = \frac{D_{i,m}}{\bar{v}_z}\left(\frac{1}{r}\frac{\partial C_i}{\partial r} + \frac{\partial^2 C_i}{\partial r^2}\right) - C_i\frac{1}{\bar{v}_z}\frac{d\bar{v}_z}{dz} \tag{14}$$

Where $D_{i,m}$ is the mixture diffusion coefficient and $\bar{v}_z$ is the mean molar axial velocity along the section. As boundary conditions, the concentration at the beginning of the reactor, z = 0, is equal to the feed concentration $C_{i,0}$ (Equation 15). Given the thin catalyst layer, the molar flux toward the catalyst surface is assumed to be equal to the kinetic rate $r_{kin,i}$ (Equation 16), and diffusion contribution within the pores for the solid phase is included in the kinetic terms (see Eqs 7,9). Finally, the zero-flux condition is imposed at the outer radius (Equation 17).

$$BC: \begin{cases} z = 0\ \forall r\ C_i = C_{i,0} & (15) \\ r = R_{int}\ \forall z\ \ -D_{i,m}\dfrac{\partial C_i}{\partial r} = r_{kin,i}\ g & (16) \\ r = R_{out}\ \forall z\ \dfrac{\partial C_i}{\partial r} = 0 & (17) \end{cases}$$

Table 1

Kinetic parameters of the reaction model by Xu and Froment [16].

Parameter	Value	Units	Notes
k_{SMR,T_r}	1.842e-4	kmol bar^{0,5} kg$_{cat}^{-1}$ h^{-1}	$T_r = 648K$
k_{WGS,T_r}	7.558	kmol bar^{-1} kg$_{cat}^{-1}$ h^{-1}	$T_r = 648K$
k_{GRR,T_r}	2.193e-5	kmol bar^{0,5} kg$_{cat}^{-1}$ h^{-1}	$T_r = 648K$
E_{SMR}	240.1	kJ mol^{-1}	-
E_{WGS}	67.13	kJ mol^{-1}	-
E_{GRR}	243.9	kJ mol^{-1}	-
K_{ads,CH_4,T_r}	0.1791	bar^{-1}	$T_r = 823K$
K_{ads,CO,T_r}	40.91	bar^{-1}	$T_r = 648K$
K_{ads,H_2,T_r}	0.02960	bar^{-1}	$T_r = 648K$
K_{ads,H_2O,T_r}	0.4152	-	$T_r = 823K$
$\Delta H_{ads,CH_4}$	-38.28	kJ mol^{-1}	-
$\Delta H_{ads,CO}$	-70.65	kJ mol^{-1}	-
$\Delta H_{ads,H_2}$	-82.90	kJ mol^{-1}	-
$\Delta H_{ads,H_2O}$	88.68	kJ mol^{-1}	-

2.4. Energy balance

One-dimensional energy balances are considered in this model for both the gas and the solid phase. Regarding the radial contributions, they are accounted for at a "macroscopic" level, meaning their derivatives are calculated only at the domain boundaries (r = R_{out} and r = R_{int}) and not at every radial point along the system. Since the reaction does not occur in the gas phase, the temperature profile along the radial direction of the gas mixture is primarily influenced by heat transfer phenomena. However, since the thermal conductivity of a gas mixture is much lower than that of a solid, this influence is minimal, resulting in only a small effect on the catalyst temperature and consequently on the reaction rate.

2.4.1. Energy balance in the gas phase

The general form of the energy balance is as follows (Eq. 18)

$$\frac{\partial Ch}{\partial t} = -\nabla\cdot(C\bar{v}_z h) - \nabla\cdot q + Q_{reaction} \tag{18}$$

Assuming steady state and no heat of reaction (Eq. 19):

$$0 = \nabla\cdot(C\bar{v}_z h) + \nabla\cdot q \tag{19}$$

At the assumptions already defined in the previous paragraph, the following are considered for the energy balance in the gas phase:

- Radiation contribution is neglected
- The axial contribution of the heat flux is mainly convection

The final form of the energy balance is in Eq. 20.

$$\frac{\partial}{\partial z}(C\bar{v}_z h) = -\frac{1}{r}\frac{\partial}{\partial r}(rC\bar{v}_z h) - \frac{1}{r}\frac{\partial}{\partial r}(rq_r) \tag{20}$$

h is the molar enthalpy of the gas flux and q_r is the radial heat flux, defined as in Eqs 21 and 22.

$$h = C_{p,gas}(T - 298.15K) \tag{21}$$

$$q_r = h_T(T - T_{cat}) \tag{22}$$

With T_{cat} being the catalyst temperature, h_T the heat transfer coefficient, defined as in Appendix A.4, and $C_{p,gas}$ is the average specific heat capacity of the gas flow, calculated as in Appendix A.3. Boundary condition is shown in Eq. 23.

$$BC:\ \ z = 0\ T = T_0 \tag{23}$$

2.4.2. Energy balance in the solid phase

A one direction energy balance has been implemented for the solid phase. The phenomena that are taken into account are

- The heat transfer from and to the gas
- The radial conductive heating from the coil
- The enthalpy terms related to the material streams of reactants
- The heat of the reactions

Assuming velocity in the axial direction is negligible, the final form of the energy balance in the solid phase is shown in Eq. 24.

$$0 = -\frac{1}{r}\frac{\partial}{\partial r}(rCv_z h) - \frac{\partial q_z}{\partial z} - \frac{1}{r}\frac{\partial}{\partial r}(rq_r) - \rho_s\sum_i r_i\Delta H_i \tag{24}$$

With ρ$_s$ being the solid bulk density, r_i the kinetic rate of the i-th reaction and ΔH_i the specific enthalpy of the i-th reaction. A zero-flux condition is imposed at the entrance and at the exit of the reactor for the boundary conditions in the axial direction (Eqs 25 and 26).

$$BC: \begin{cases} z = 0 \quad \dfrac{\partial T}{\partial z} = 0 & (25) \\ z = L \quad \dfrac{\partial T}{\partial z} = 0 & (26) \end{cases}$$

2.5. Numerical solution approach

In order to evaluate the performance of the reactor, the methane conversion (Eq. 27) and the hydrogen yield (Eq. 28) are calculated as follows:

$$X_{CH_4}(z) = \frac{Q_{z,0}C_{CH_4,0} - \overline{Q}_z(z)\overline{C}_{CH_4}(z)}{Q_{z,0}C_{CH_4,0}} \tag{27}$$

$$Y_{H_2}(z) = \frac{\overline{Q}_z(z)\overline{C}_{H_2}(z)}{Q_{z,0}C_{CH_4,0}} \tag{28}$$

where $\overline{Q}_z$, $\overline{C}_{CH_4}$, and $\overline{C}_{H_2}$ represent the volumetric flow rate, methane concentration, and hydrogen concentration along the section, respectively.

The solution of mass balance Eq. 14 is based on a finite difference approach. The two coordinates of the system were discretized into a finite number of points (r_{pts} and z_{pts} with index k and i respectively), while the derivatives have been approximated with conventional finite difference schemes. respectively), while the derivatives have been approximated with conventional finite difference schemes. A forward scheme has been employed for first derivatives, while a centered scheme has been chosen to approximate second derivatives. Regarding the right-hand side of the equation, it is calculated in the forward point in z (index i + 1). After discretization, the material balance becomes as in Eq. 29:

$$\frac{C_k^{i+1} - C_k^i}{\Delta z} = \frac{D_{i,m}}{\overline{v}_z}\left(\frac{1}{r_k}\frac{C_{k+1}^{i+1} - C_k^{i+1}}{\Delta r} + \frac{C_{k+1}^{i+1} - 2C_k^{i+1} + C_{k-1}^{i+1}}{\Delta r^2}\right) - C_k^{i+1}\frac{1}{\overline{v}_z}\frac{d\overline{v}_z}{dz} \tag{29}$$

Which, after collecting the terms C_{k+1}^{i+1}, C_k^{i+1} and C_{k-1}^{i+1} and implementing the discrete form of the boundary conditions, leads to a system of equations for every z point in the form (Eq. 30):

$$C^i = \underline{A}\cdot C^{i+1} + a \tag{30}$$

This system is solved by inversion of the matrix of coefficients $\underline{A}$ to find the radial array of concentrations C^{i+1} from the one in the previous z point C^i and the vector of known terms a. Velocity and its derivative were initially guessed and iteratively updated until convergence was achieved.

The energy balance equations (Eqs 20 and 24) have been manipulated in order to get to a form which explicitly depends on temperature, the variable of interest.

The numerical solution of Eqs 20 and 24 was implemented using the Python routines *solve_ivp* and *solve_bvp* [18].

3. Results and discussion

The goal of the mathematical model is to determine which set of operating conditions and geometric parameters best meet the hydrogen production requirements of the system. In addition, it provides insights into the overall behavior of the reactor in various scenarios. In the following sections, a base case scenario is reported with its performance in terms of temperature, species concentrations, conversion and hydrogen selectivity profiles along the reactor. Subsequently, a parametric analysis is conducted, in which different cases are compared by varying a single parameter while keeping all other operating conditions constant. The analysis focuses on the influence of the following parameters: gas inlet temperature, heating coil temperature and reactor outer radius.

3.1. Base case scenario

The results from a base case are reported as a benchmark for the comparison of the parametric analysis. The conditions selected are shown in Table 2. The inlet concentration composition is defined with the assumption that the steam-to-carbon ratio is equal to 4.

Important insights into methane consumption can be derived from its molar fraction profile along the axial and radial directions, as shown in Fig. 3. The figure highlights that most of the reactant is consumed within the first few centimeters of the reactor axis. This behavior is primarily due to the small geometry of the system, wherein a fixed velocity and a fixed inlet concentration result in a low inlet methane flowrate. However, that the concentration tends to be higher at $r = R_{out}$ than at $r = R_{int}$. This occurs because the gas fed into the outermost region, which is farthest from the catalyst, needs sufficient time to diffuse radially, reach the catalyst surface and react. This means that the outer radius for a single module, and therefore radial diffusion, are critical factors to consider when evaluating reactor performance.

In Fig. 4 the molar fractions of all species along z are reported and a significant slope in the curves at z = 0 is noticeable. This occurs due to the combined effects of both thermodynamic and kinetic phenomena. The thermodynamic contribution arises from the feed being far from the equilibrium composition at T_{cat} (z = 0), due to the high concentration of reactants in the feed, which strongly accelerates the reaction. As the axial length increases, the system gradually approaches the equilibrium composition, resulting in a flattening of the slope.

Further insights can be gained by directly comparing the solid and gas temperature profiles in Fig. 5. In the initial sections of the reactor, the solid phase is getting cooled due to the endothermic nature of the reactions, which occurs mainly in the inlet zone. However, the solid temperature quickly stabilizes at the same value as T_{coil}, as the reactions become the only factor lowering the system's temperature. Once equilibrium is reached, the system undergoes only a temperature rise. Regarding the gas temperature, it consistently increases throughout the reactor. Initially, the slope of the gas temperature profile is steep because the reactants enter at a lower temperature and exit as products at a higher temperature. In later stages, when the reaction slows down, the gas temperature increases only due to convective heat transfer, which is a slower process. Consequently, the rate of temperature rise decreases. Finally, it is possible to notice that the gas exits the reactor at a significantly lower temperature than the solid. This discrepancy highlights the system's thermal dynamics and the efficiency of heat transfer mechanisms in electrifying the solid compared to the gas phase.

Finally, methane conversion is one of the most important aspects for evaluating reactor performance. In the standard case, the conversion profile along the axis of the reactor is the one in Fig. 6. The conversion

Table 2
Base case scenario parameters and operative conditions.

Parameter	Description	Value	Units
R_{coil}	Radius from the central axis of the reactor to the surface of the heating coil	4e-3	m
R_{int}	Radius from the central axis of the reactor to the surface of the catalyst	5e-3	m
R_{out}	Radius from the central axis -1of the reactor to the outer side of the gas domain	7.5e-3	m
L	Total length of the reactor	1	m
T_0	Inlet gas temperature	550	°C
T_{coil}	Heating coil temperature	800	°C
$v_{z,0}$	Initial gas velocity	5	m s^{-1}
$y_{CH_4,0}$	Inlet molar fraction of CH_4	0.19	-
$y_{H_2O,0}$	Inlet molar fraction of H_2O	0.774	-
$y_{CO,0}$	Inlet molar fraction of CO	0.016	-
$y_{CO_2,0}$	Inlet molar fraction of CO_2	0	-
$y_{H_2,0}$	Inlet molar fraction of H_2	0.016	-

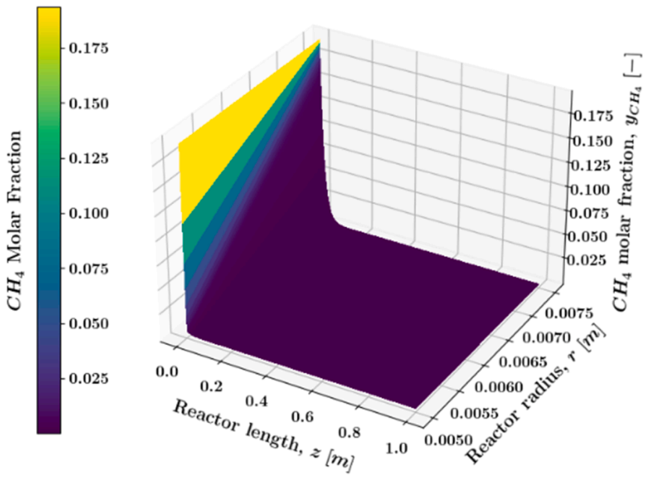

Fig. 3. 3D methane molar fraction profile in the gas phase of the reactor, base case scenario.

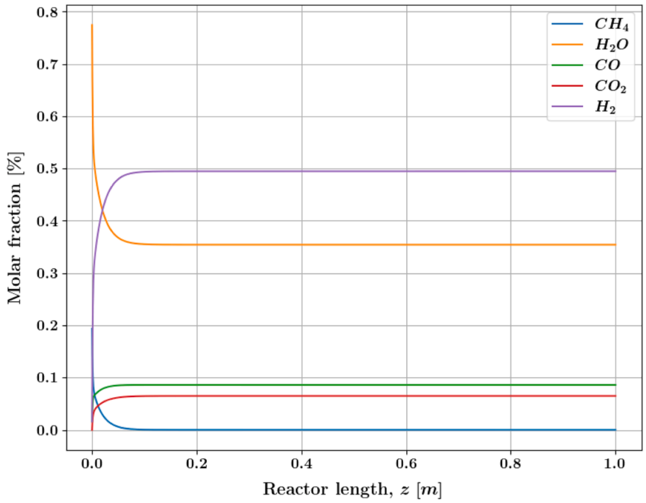

Fig. 4. Radial mean molar fraction profiles along the z coordinate of the reactor, base case scenario.

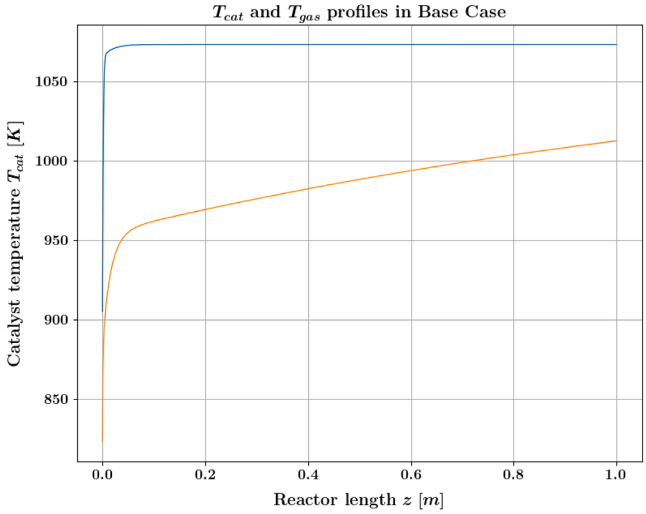

Fig. 5. Direct comparison between the solid and gas temperature profiles along the z coordinate of the reactor, base case scenario.

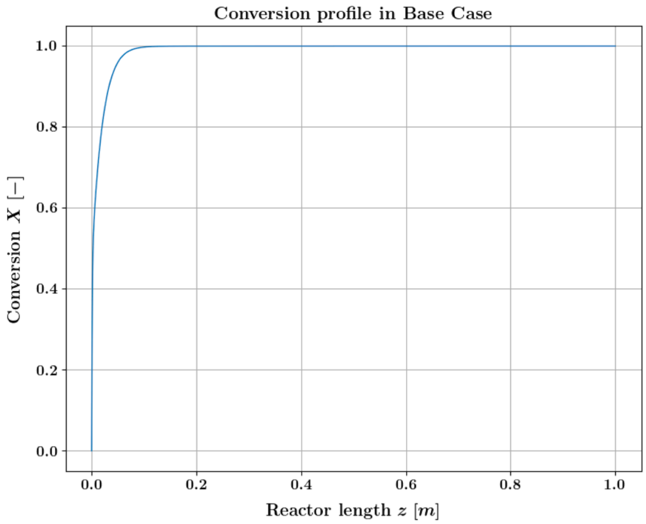

Fig. 6. Conversion profile along the z coordinate of the reactor, base case scenario.

rises and gets to the equilibrium very quickly, approximately after 10 cm. For this reason, the reactor appears to be significantly oversized for the base case scenario, since its length is much larger than the required value to achieve full conversion. Thus, a large portion of the reactor remains unused.

3.2. Gas inlet temperature variation

In this section the inlet gas temperature is changed from 300°C to 800°C with intervals of 100°C. Two sub cases are analyzed: one with a T_{coil} of 650°C (named “low temperature") and one with T_{coil} of 800°C (named “high temperature"). This parametric study allows the identification of the potential productivity and the optimal operating temperature, both critical factors for process optimization. This is an important aspect for process optimization, mainly due to the energy savings which may derive from a lower coil temperature, or from the opportunity to work with a feed as cold as possible while still maintaining product specifications.

3.2.1. Low coil temperature

In terms of molar fraction profiles, the main difference lies in the first sections of the reactor, as it is reported in Fig. 7.

The profile at the lower gas inlet temperature shows a smoother slope, while the profile at 800°C is significantly steeper. This behavior is primarily driven by the temperature dependence of the reaction kinetics. Since the reaction takes place in the solid phase, a hotter flow of reactants promotes faster reaction rates, while lower gas inlet temperatures cool the solid phase, resulting in a lower methane consumption rate. In addition, mass transport limitations play a significant role. At lower temperatures, the diffusion coefficient decreases, leading to less efficient diffusion of reactants toward the catalyst. Therefore, the profile differences are influenced by both kinetics, which reduces the radial concentration gradient, and mass transport, which slows down the diffusion of reactants. To achieve equilibrium at lower temperatures, a longer reactor length is required.

The gas temperature profile, as shown in Fig. 8, is consistent with the previously discussed observations. At low inlet temperatures, the gas takes longer to heat up, which directly affects both the solid phase reaction rate and the diffusion coefficient. A key aspect is the notable difference in the slopes of the profiles. In cases where $T_0 > T_{coil}$, the gas is cooled by the flow of reactants exiting the catalyst at a lower temperature and gradually approaches the catalyst temperature from above. In contrast, if $T_0 < T_{coil}$, the gas heats up and stabilizes at T_{coil} in a shorter

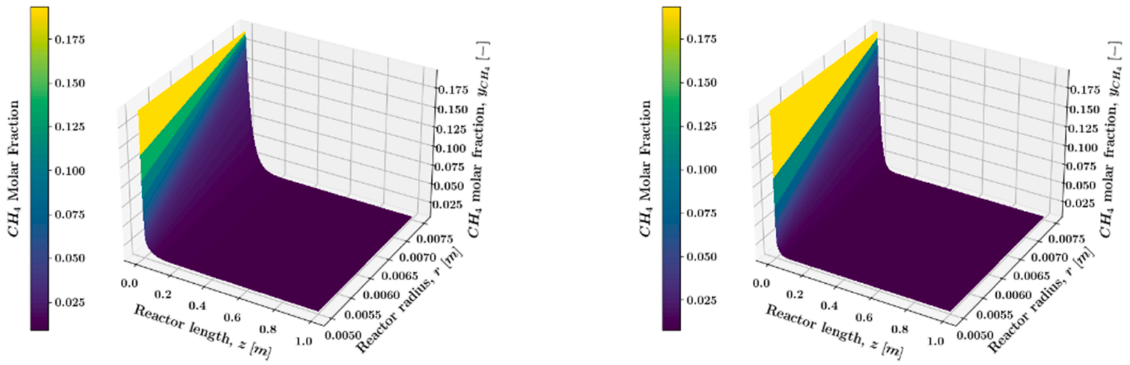

a) b)

Fig. 7. 3D methane molar fraction profile of the reactor at $T_{coil} = 650°C$ and $T_0 = 300°C$ (a) and $T_0 = 800°C$ (b).

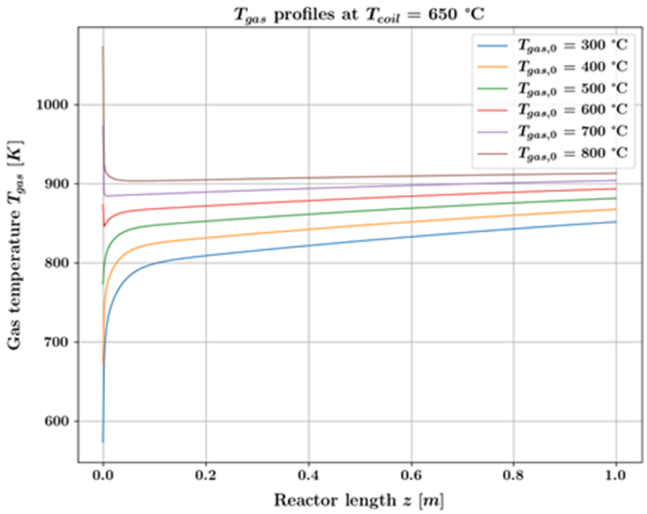

Fig. 8. Gas temperature profiles along the z coordinate at different T_0 and $T_{coil} = 650°C$.

distance.

Furthermore, the outlet temperature of the gas varies significantly at different inlet temperatures, as shown in Fig. 8. This difference has important implications for the operating conditions of the MCFC system, as the ideal scenario would be to achieve an outlet temperature of approximately 580°C [19–21] while maintaining high conversion levels. However, these two goals are in conflict. The best balance between the temperature requirements and conversion efficiency needs to be reached. On the other hand, outlet conversion is not equally affected by T_0. In fact, considering Fig. 9, all curves settle at values between 92% and 95% before the end of the reactor length, which corresponds to the thermodynamic equilibrium at this specific coil temperature. In all cases, a length of 1 m has been assumed to observe the differences under various operating conditions. However, it is evident that this length is excessive for all scenarios, as the conversion is thermodynamically limited only by the value of T_{coil}. On the other hand, the solid catalyst temperature is weakly affected by the differences in inlet T . Indeed, the curves overlap almost perfectly, with small differences in the first few cm of the reactor length (Fig. 9).

3.2.2. *High coil temperature*

Methane molar fraction for $T_{coil} = 800°C$ can be seen in Fig. 10.

As the previous case, the axial slope of the curve is gentler at low T_0. However, it is possible to evaluate the impact of T_{coil}. Compared to the previous case with $T_{coil} = 650°C$, methane molar fraction is lower in every point along the reactor. This is a direct result of the more favorable kinetics in the solid phase, which enhance the radial concentration gradient and, consequently, improve mass transport.

The analysis of the gas temperature profiles in Fig. 11 reveals

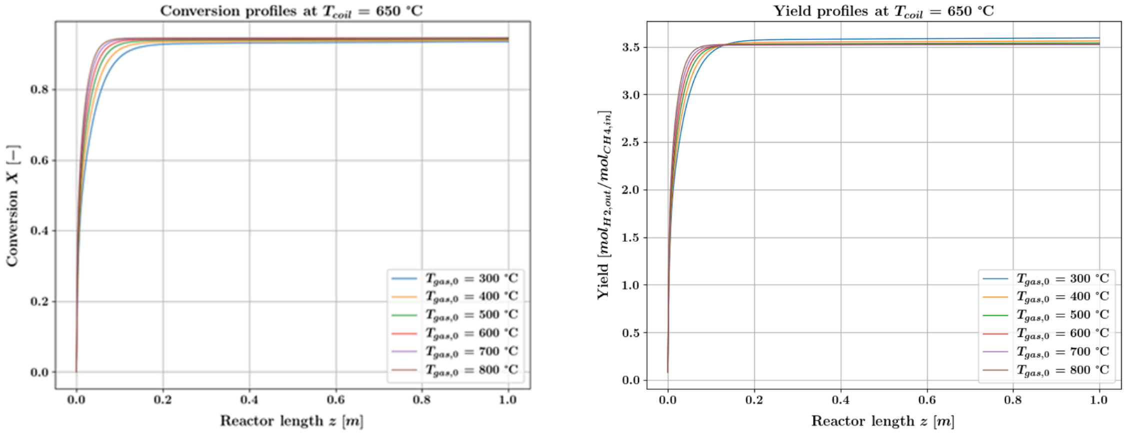

a) b)

Fig. 9. Methane conversion (a) and hydrogen yield (b) profiles along the z coordinate at different T_0 and $T_{coil} = 650°C$.

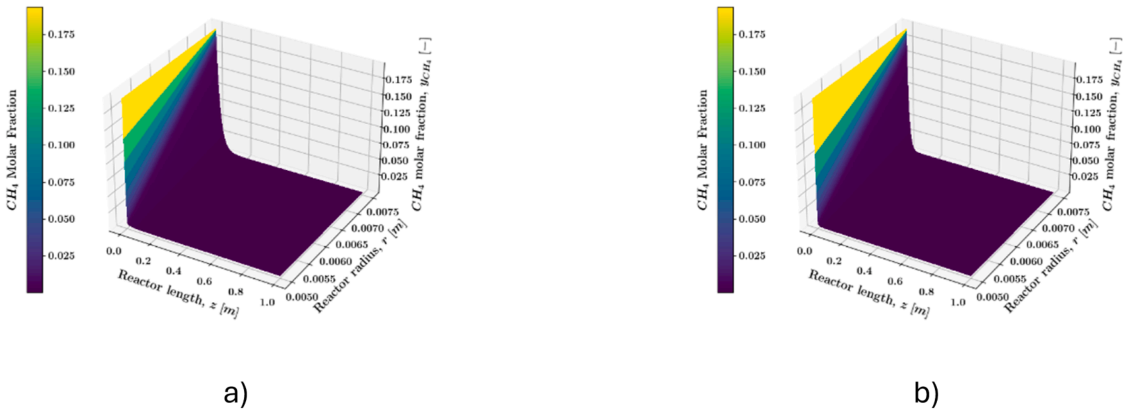

Fig. 10. 3D methane molar fraction profile of the reactor at T_{coil} = 800°C and T_0= 300°C (a) and T_0= 800°C (b).

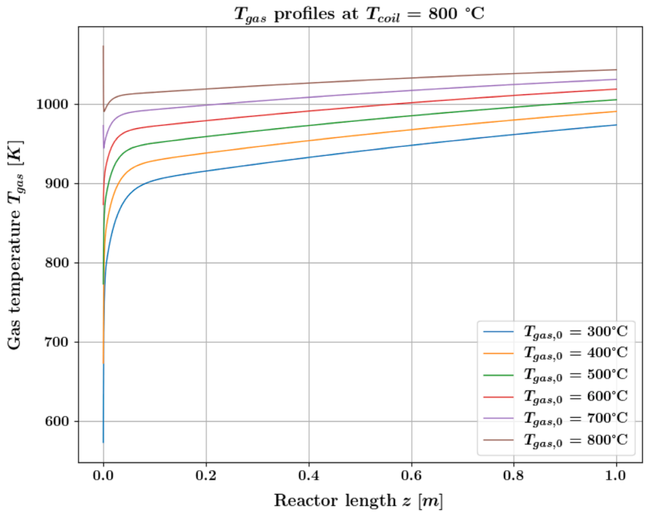

Fig. 11. Gas temperature profiles along the z coordinate for different T_0 and T_{coil} = 800°C.

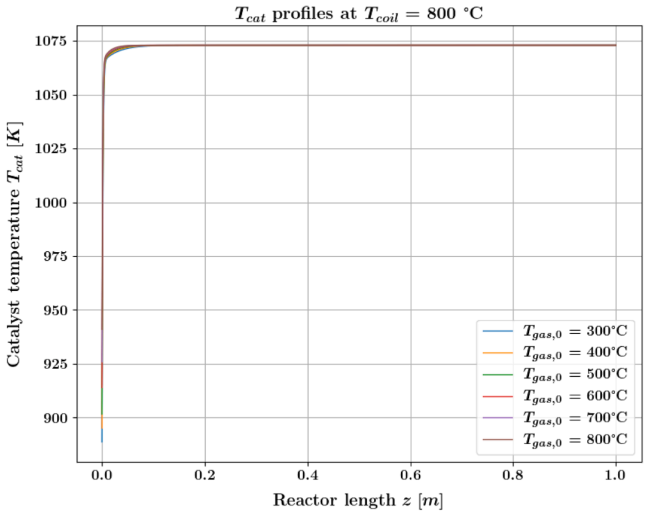

Fig. 12. Catalyst temperature profiles along the z coordinate for different T_0 and T_{coil} = 800°C.

different behaviors depending on the inlet temperature. For cases where $T_0 < 700$°C, the temperature curves exhibit a consistent upward trend. In contrast, at higher T_0, the profiles initially show a fast drop before reaching a steady asymptotic rise, approaching T_{coil}. This behavior is attributed to the rapid endothermic reaction occurring in the initial section of the reactor, which absorbs a significant portion of the heat supplied by the hot gas at the inlet, especially at higher temperatures, where the reaction is favored.

Again, under these conditions, the temperature profiles of the catalyst are almost the same, varying the inlet temperature, as shown in Fig. 12.

Regarding methane conversion and hydrogen yield, the different profiles are reported in Fig. 13. The value of T_{coil} is the most important parameter, since the thermodynamic equilibrium composition is the limiting factor. In fact, in all these cases, the final value of conversion is close to 100%, achieved in a length of about 20 cm, since the equilibrium conversion limit is higher.

3.3. Heating coil temperature variation

Another important parameter for the design stage of the reactor is the coil temperature T_{coil}. Indeed, the aim of this section is to investigate its influence on the performance of the reactor, with particular interest in finding the overall best compromise between the necessary heat throughput in order to get a satisfactory conversion, and the economic aspects related to the electrical energy required for its operation. Six runs have been performed, each of these with an increasing T_{coil} from 550°C to 800°C, with steps of 50°C. Regarding the gas inlet temperature, it was set to a constant value of 550°C.

Regarding its effect on molar fraction profiles, higher T_{coil} values enhance reaction kinetics, promoting a greater radial concentration gradient that facilitates species diffusion to and from the catalyst. Fig. 14 compares the two extreme cases in this analysis, T_{coil}= 550°C and 800°C. As observed in the previous cases, the outer radial point exhibits a higher concentration, attributed to the time required for the reactant to diffuse toward the catalyst surface. It is important to note that, at low T_{coil}, the decrease in concentration along the z axis is much less significant compared to that seen at higher T_{coil} values. This is because at lower temperatures the equilibrium is less shifted toward the products. This reduces the driving force for reactant consumption, which leads to a less pronounced decline in concentration along the reactor.

The gas temperature profiles are strongly affected by the coil temperature, as shown in Fig. 15. For cases where $T_0 < T_{coil}$, the profiles exhibit an initial steep gradient followed by a more moderate, linear increase. In addition, the initial slope of the temperature increase is consistent across all scenarios, regardless of the coil temperature. This uniformity likely arises because the higher solid temperature sustains a reaction rate that evenly heats the gas per unit length. Once mass transport or equilibrium limitations are reached, the slope decreases, and the temperature rise slows. Finally, in the specific scenario where T_0

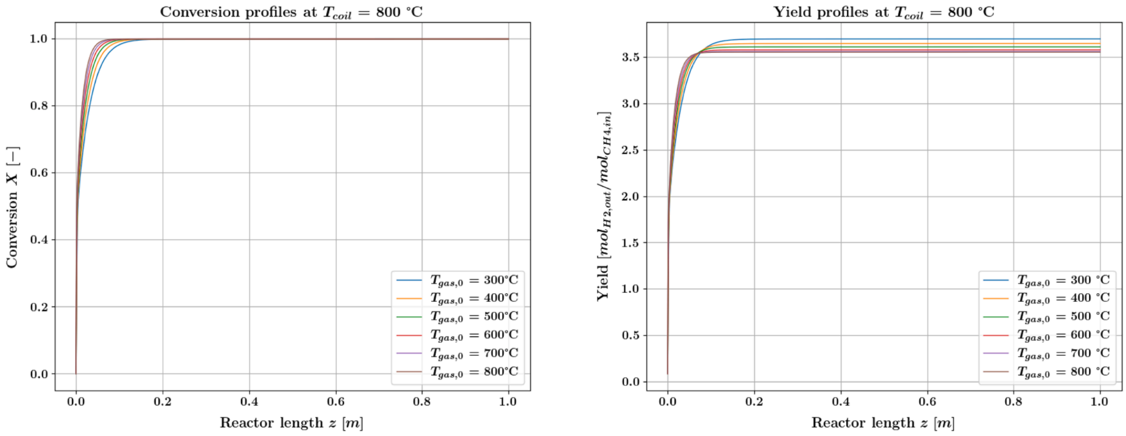

a) b)

Fig. 13. Methane conversion (a) and hydrogen yield (b) profiles along the z coordinate at different T_0 and $T_{coil} = 800°C$.

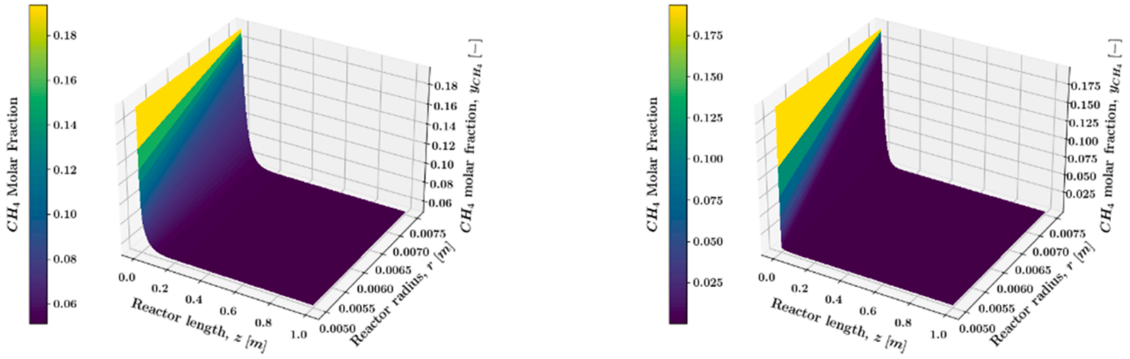

a) b)

Fig. 14. 3D methane molar fraction profile of the reactor at T_0= 550°C and T_{coil} = 550°C (a) and T_{coil}= 800°C (b).

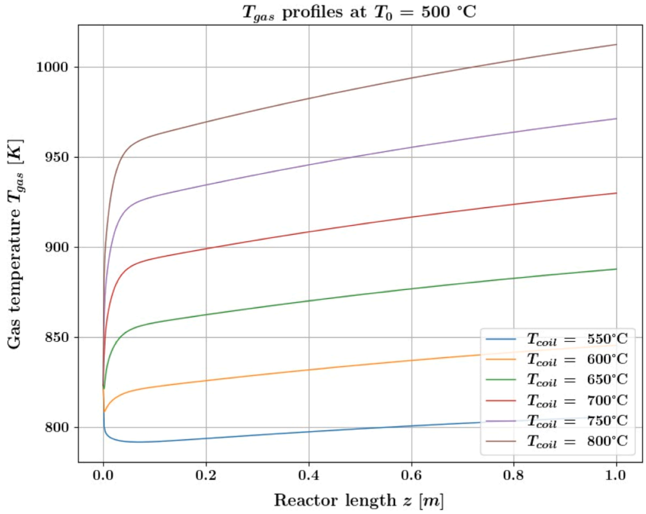

Fig. 15. Gas temperature profiles along the z coordinate at different T_{coil} and $T_0 = 550°C$.

$= T_{coil}$, the profile initially shows a decrease before gradually increasing and asymptotically approaching T_{coil}. This behavior highlights the interactive effect between the gas-solid temperature exchange and the endothermic reaction within the catalyst, which takes place only in the initial part of the reactor length.

The solid's temperature profiles, reported in Fig. 16, have an overall

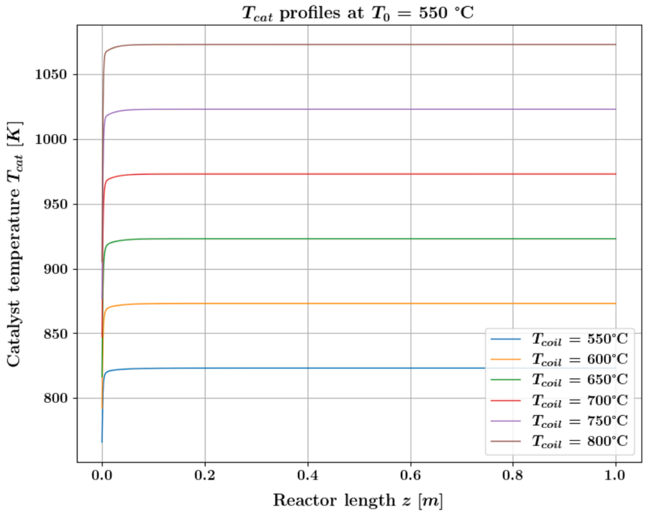

Fig. 16. Catalyst temperature profiles along the z coordinate at different T_{coil} and $T_0 = 550°C$.

trend which is the same as in all cases: a fast, almost vertical, increase at the beginning followed by a flat slope once T_{coil} has been achieved. Specifically, at higher T_{coil}, the initial temperature drop caused by the endothermicity of the reaction increases. This is because higher temperatures favor reaction kinetics, leading to a higher reaction rate and consequently more heat being absorbed from the solid. As a result, a higher T_{coil} corresponds to a larger initial temperature difference (ΔT), a critical consideration for material selection, which must be able to withstand such thermal stresses.

In conclusion, Fig. 17 shows the conversion and yield profiles in all these cases. The relevance of T_{coil} lies in its direct influence on the equilibrium methane conversion limit. Of course, as T_{coil} increases, the maximum achievable conversion increases, since the SMR reaction is favored by high temperatures, with a directly related increase in yield. However, at atmospheric pressure, methane equilibrium conversion exceeds 95% at 700°C. Therefore, operating with a T_{coil} above this temperature may not be efficient, as the marginal gain in conversion does not justify the additional energy consumption.

3.4. Outer radius variation

In this section, a parametric analysis on the influence of the outer radius R_{out} is presented. Particularly, the outer radius is varied by introducing a corrective factor *f*, define as:

$$R_{out} = R_{out,0} \cdot f \tag{25}$$

Where $R_{out,0}$is the value used in the reference case (7.5e-3 m). The values taken for f are: 1, 1.5, 1.8, 2.1, 2.4, 2.7 and 3.

The information gained from this analysis is important for the determination of the most appropriate tube pitch, which corresponds to twice the value of Rout, as shown in Fig. 1. It is important to determine the conversion as a function of the pitch in order to define when the radial diffusive transport of the reactants toward the catalyst surface becomes a limiting phenomenon for the reactor performance. The evaluation of the pitch influences the choice of the number of modules necessary to achieve the desired productivity and, consequently, the energy consumption of the reformer. In fact, a small number of modules means less energy required. On the other hand, if the pitch is too large, the gas takes more time to reach the catalyst and the total catalyst specific surface area decreases and may not be sufficient to convert all the gas.

An important aspect can be seen from Fig. 18 which shows CH_4 molar fraction profiles for *f* values of 1 and 3, representing the extremes of the studied range. In fact, since the initial velocity of the inlet is fixed, the variation of the outer radius results in a greater molar flow. As a consequence, with larger gas sections, the amount of treated reactants and mass transport resistances increase. For this reason, the axial slope of the curves (at r = R_{out}) decreases as *f* gets larger.

Additionally, the presence of a radial concentration gradient is the main driving force which allows the reactants at r = R_{out} to diffuse toward the catalyst and react. At this point, the only way to achieve greater conversion would be to increase the coil temperature to favor reaction kinetics, making the concentration gradient steeper. In the case reported in Fig. 18 (a) equilibrium has been reached, while in Fig. 18 (b) a longer reactor would allow for a higher conversion, since the radial slope indicates that there still is some unreacted methane.

As reported in Fig. 19, it is evident that the temperature rise is much more moderate for larger values of *f*. A larger gas feed increases thermal inertia, requiring more heat input to reach a given temperature difference. Secondly, a greater amount of methane means a greater amount of heat is removed from the system due to the endothermic nature of the reaction. As a result, not only does temperature rise at a lower rate because it takes longer to heat a larger volume of gas, but also because the gas continues to react, slowing the heating process even further. Therefore, except for low values of *f*, where complete conversion is achieved in the initial section of the reactor, the higher the *f*, the lower the slope of the temperature rise.

Methane conversion and hydrogen yield profiles, as expected, exhibit significant variation depending on the geometry. As illustrated in Fig. 20, larger modules (higher *f* values) fail to reach equilibrium conversion, unlike smaller modules, which achieve it. This difference is directly linked to the amount of CH_4 introduced into the reactor. Although equilibrium is rapidly reached at r = R_{int} in all cases, larger modules feed more methane into the system, and the increased distance the gas must cover to react presents additional challenges. Therefore, for higher *f* values, a longer reactor is required to ensure sufficient residence time for equilibrium conversion.

4. Conclusions

In response to the global climate crisis, the European Green Deal aims to reduce greenhouse gas emissions by 50% by 2030 and achieve carbon neutrality by 2050. The maritime sector, responsible for 3-4% of global emissions, is now subject to stricter regulations, including the EU ETS reform in 2023. To support decarbonization, this study focuses on the integration of MCFC onboard technology for simultaneous power generation and CO_2 capture from ship exhaust. A key challenge is to ensure a continuous supply of hydrogen, for which Electrified Steam Methane Reforming (eSMR) is a promising efficient and compact solution. Through modeling simulations, key operating parameters such as

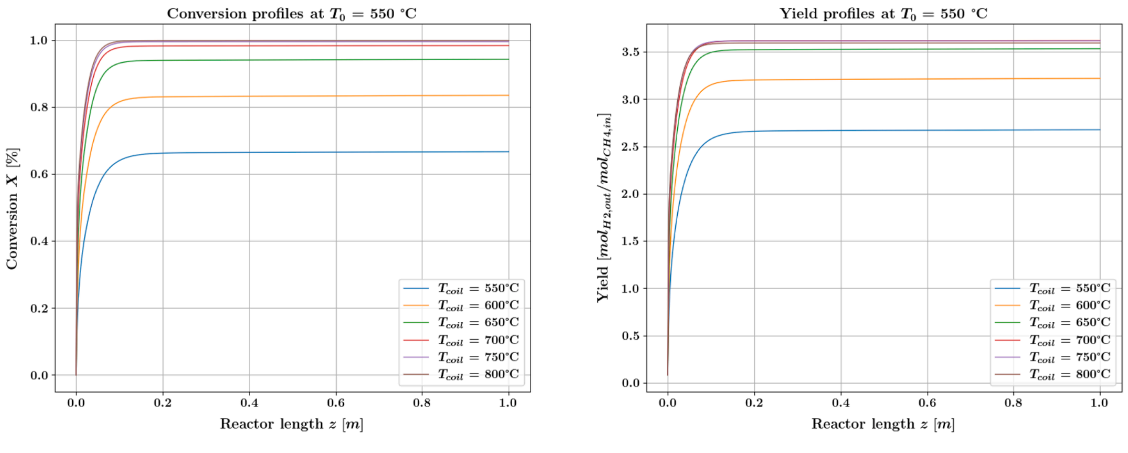

a) b)

Fig. 17. Methane conversion (a) and hydrogen yield (b) profiles along the z coordinate at different T_{coil} and T_0 = 550°C.

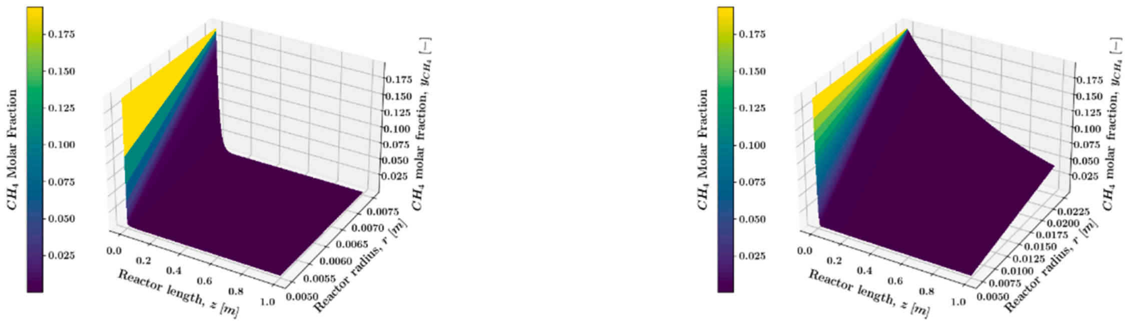

a) b)

Fig. 18. 3D methane molar fraction profile of the reactor with $f = 1$ (a) and $f = 3$ (b).

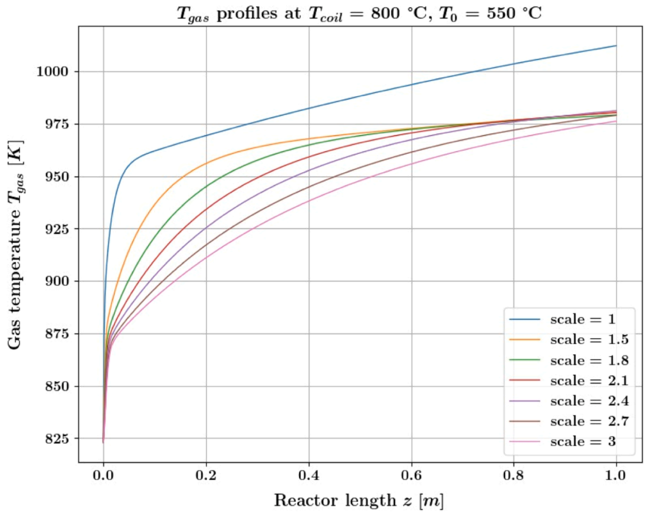

Fig. 19. Gas temperature profiles along the z coordinate at different f values, $T_{coil} = 800^{\circ}$C, $T_0 = 550^{\circ}$C.

gas inlet temperature, coil temperature and reactor geometry are analyzed to determine optimal conditions.

A mathematical model has been developed to elucidate the operating principles of the system, identifying critical parameters and optimal working conditions. The reactor geometry is based on a "shell and tube" configuration, in which a single module is assumed as a concentric annular pipe (tube-in-tube configuration). The model was then implemented in Python to solve mass and energy balance equations for both the gas and solid phases of the reactor.

The results confirm the potential of this concept, primarily due to its compact design and high conversion efficiency. The reactor showed excellent performance in almost all cases, reaching equilibrium within the first half of its length. Pitch distance analysis revealed that radial diffusion of reactants toward the catalyst surface was the primary limiting factor. In contrast, the gas inlet temperature had minimal effect, as the direct contact of the catalyst with the heating zone ensures that the reactants quickly reach the catalyst temperature, thereby enhancing the reaction kinetics. For this reason, the two most influential parameters in tihs study were the heating coil temperature (T_{coil}), which determines the equilibrium conditions and the outlet composition, and the outer radius (R_{out}), which significantly impacts conversion by determining the radial distance the gas must diffuse to reach the catalyst surface and react.

As an example, the power required for the reference case was calculated and found to be approximately 370 Watts. When related to hydrogen production, this results in a value of approximately 10 kWh per kilogram of hydrogen produced.

In summary, the resistive reformer demonstrated good performance, and its characteristics fit well with the requirements of an MCFC process, making the eSMR configuration studied in this work a promising solution to supply hydrogen to the fuel cell in onboard applications.

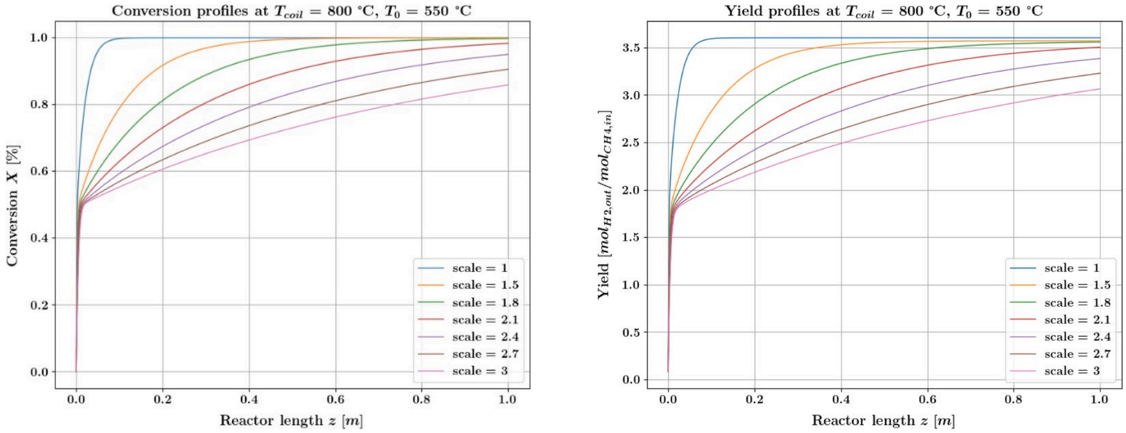

a) b)

Fig. 20. Methane conversion (a) and hydrogen yield (b) profiles along the z coordinate at different f values, and $T_{coil} = 800^{\circ}$C, T_0= 550°C.

CRediT authorship contribution statement

Stefano Moriggi: Writing – original draft, Software, Resources, Methodology, Investigation, Data curation, Conceptualization. **Daniela De Cata:** Writing – review & editing, Resources, Methodology, Investigation, Data curation. **Dario Bove:** Writing – review & editing, Validation, Supervision, Resources, Methodology, Conceptualization. **Barbara Bosio:** Writing – review & editing, Supervision, Project administration, Methodology, Conceptualization.

Declaration of competing interest

The authors declare the following financial interests/personal relationships which may be considered as potential competing interests:

Dario Bove reports financial support was provided by European Union NextGenerationEU. If there are other authors, they declare that they have no known competing financial interests or personal relationships that could have appeared to influence the work reported in this paper.

Acknowledgments

This research was partially developed within the project “Network 4 Energy Sustainable Transition—NEST” funded under the National Recovery and Resilience Plan (NRRP), Mission 4 Component 2 505 27 506 Investment 1.3—Call for tender No. 1561 of 11.10.2022 of Ministero dell’Università e della Ricerca (MUR); 507 508 funded by the European Union—NextGenerationEU.

Appendix A. Calculation of physicochemical properties

A.1. Average axial velocity

Due to the already mentioned plug-flow assumption, the axial velocity is considered as a function of the axial coordinate only, while it is constant along the radial direction. The basic formula is:

$$\overline{v}_z(z) = \frac{\overline{Q}_z(z)}{A} \tag{A.1}$$

Where $\overline{Q}_z(z)$ is the volumetric flowrate in the annular space, while A is the cross-sectional area. Therefore, to calculate $v_z(z)$ an expression for $\overline{Q}_z(z)$ is needed. The general formula takes into account the dependence on temperature, pressure and the presence of reactions [22]:

$$\overline{Q}_z(z) = Q_{z,0}\frac{T(z)}{T_0}\frac{P_0}{P(z)}\left(1 + \varepsilon\,\overline{X}(z)\right) \tag{A.2}$$

Wherein ε is a coefficient taking into account the stoichiometry of the reaction and $\overline{X}(z)$ is the molar fractional conversion of the reference reactant (methane in this case), calculated as:

$$\overline{X}(z) = \frac{Q_{z,0}C_{CH_4,0} - \overline{Q}_z(z)\overline{C}_{CH_4}(z)}{Q_{z,0}C_{CH_4,0}} \tag{A.3}$$

Substituting Equation A.3 into Equation A.2, an explicit formulation can be obtained for $\overline{Q}_z(z)$. Then, the final equation for $v_z(z)$, with constant pressure hypothesis, results to be:

$$\overline{v}_z(z) = \frac{\overline{Q}_z(z)}{A} = \frac{Q_{z,0}\frac{T(z)}{T_0}(1+\varepsilon)}{A\left(1 + \frac{T(z)}{T_0}\,\frac{\overline{C}_{CH_4}(z)}{C_{CH_4,0}}\varepsilon\right)} \tag{A.4}$$

A.2. Material diffusivity

As it is common in literature, the Chapman-Enskog theory, based on the kinetic theory of gases, has been used to calculate the binary diffusion coefficients of the mixtures given by the binary combination of all the species [23]. Equation A.5 reports its formulation.

$$\mathrm{D}_{AB} = 1.86{\cdot}10^{-3}\frac{T^{3/2}}{p\sigma_{AB}^2 MW_{AB}^2 \Omega_D} \tag{A.5}$$

Wherein σ_{AB} is the mean collision diameter, MW_{AB} is the harmonic mean of molecular weights and Ω_D is the so-called “collision integral".

After the calculation of the binary diffusion coefficient for all possible couples of compounds, the overall coefficient taken to be constant for all species is

$$\mathrm{D}_{i,\ \mathrm{mix}} = \left(\sum_i\sum_{j>1}\frac{y_i y_j}{\mathrm{D}_{ij}}\right)^{-1} \tag{A.6}$$

A.3. Specific heat

The formulation for the molar specific heat is reported in Equation A.7, which has been taken from Perry’s manual [24].

$$C_p = A + B\left(\frac{C}{T\sinh\left(\frac{C}{T}\right)}\right)^2 + B\left(\frac{E}{T\cosh\left(\frac{E}{T}\right)}\right)^2 \tag{A.7}$$

With coefficients *A, B, C, D* and *E* being relative to the specific compound.

A.4. Convective heat transfer coefficient

The heat transfer between the gas phase and the solid phase mainly occurs by convection. For this reason, a convective heat transfer coefficient has been calculated in each point along the axial direction of the reactor, accounting for the variation of properties such as fluid velocity or specific heat. This has been accomplished using the Sieder-Tate correlation for the Nusselt number, valid for pipes in the laminar regime [24].

$$Nu = 1.86\left(Re\Pr\frac{D}{L}\right)^{1/3} \tag{A.8}$$

A.5. Other parameters

Some other quantities have not been rigorously calculated. Rather, they have been estimated based on realistic values. This has been done in order to achieve a model as flexible as possible, wherein each of these quantities can be modified in order to observe what variation it leads to. In Table A.1 these parameters are reported.

Table A.1
Estimated parameters of the simulation.

Parameter	Description	Value	Units
μ	Dynamic viscosity of the gas	2e-5	Pa s
λ_g	Gas thermal conductivity	0.07	W m^{-1} K^{-1}
λ_s	Solid thermal conductivity	40	W m^{-1} K^{-1}
ρ_s	Solid bulk density	4000	kg m^{-3}

Data availability

The data that has been used is confidential.

References

[1] European Commission, The European green deal, https://commission.europa.eu/strategy-and-policy/priorities-2019-2024/european-green-deal_en, 2020 (accessed 02 March 2025).

[2] International Energy Agency, Net Zero by 2050: A roadmap for the global energy sector, 2021. https://www.iea.org/reports/net-zero-by-2050 (accessed 02 March 2025).

[3] International carbon action partnership, EU extends its ETS to the maritime sector, https://icapcarbonaction.com/en/news/eu-extends-its-ets-maritime-sector, 2024 (accessed 02 March 2025).

[4] A. Buonomano, G. Del Papa, G.F. Giuzio, R. Maka, A. Palombo, G. Russo, Design and retrofit towards zero-emission ships: decarbonization solutions for sustainable shipping, Renewable and Sustainable Energy Reviews 213 (2025) 115384, https://doi.org/10.1016/j.rser.2025.115384.

[5] B. Bosio, M. Archetti, E. Audasso, D. Bove, Process analysis of a molten carbonate fuel cell on-board application to reduce vessel CO_2 emissions, Chemical Engineering and Processing-Process Intensification 190 (2023) 109415, https://doi.org/10.1016/j.cep.2023.109415.

[6] R. Risso, L. Cardona, M. Archetti, F. Lossani, B. Bosio, D. Bove, A review of on-board carbon capture and storage techniques: solutions to the 2030 IMO regulations, Energies 16 (2023) 6748, https://doi.org/10.3390/en16186748.

[7] V. Bortuzzo, S. Bertagna, V. Bucci, Mitigation of CO_2 emissions from commercial ships: Evaluation of the technology readiness level of carbon capture systems, Energies 16 (2023) 3646, https://doi.org/10.3390/en16093646.

[8] L. Mastropasqua, M. Spinelli, A. Paganoni, S. Campanari, Preliminary design of a MW-class demo system for CO_2 capture with MCFC in a university campus cogeneration plant, Energy Procedia 126 (2017) 453–460, https://doi.org/10.1016/j.egypro.2017.08.213.

[9] D.R. Nhuchhen, S.P. Sit, D.B. Layzell, Towards net-zero emission cement and power production using molten carbonate fuel cells, Applied Energy 306 (2022) 118001, https://doi.org/10.1016/j.apenergy.2021.118001.

[10] R. Cooper, D. Bove, E. Audasso, M.C. Ferrari, B. Bosio, A feasibility assessment of a retrofit molten carbonate fuel cell coal-fired plant for flue gas CO_2 segregation, International Journal of Hydrogen Energy 46 (2021) 15024–15031, https://doi.org/10.1016/j.ijhydene.2020.09.189.

[11] S.T. Wismann, J.S. Engbæk, S.B. Vendelbo, F.B. Bendixen, W.L. Eriksen, K. Aasberg-Petersen, C. Frandsen, I. Chorkendorff, P.M. Mortensen, Electrified methane reforming: a compact approach to greener industrial hydrogen production, Science 364 (2019) 756–759, https://doi.org/10.1126/science.aaw8775.

[12] D. De Cata, L. Mazzeo, V. Piemonte, A. Giaconia, Electrified steam methane reforming as efficient pathway for sustainable hydrogen production and industrial decarbonization: A critical review, International Journal of Hydrogen Energy 105 (2025) 31–44, https://doi.org/10.1016/j.ijhydene.2025.01.202.

[13] L. Zheng, M. Ambrosetti, F. Zaio, A. Beretta, G. Groppi, E. Tronconi, Direct electrification of Rh/Al_2O_3 washcoated SiSiC foams for methane steam reforming: An experimental and modelling study, International Journal of Hydrogen Energy 48 (2023) 14681–14696, https://doi.org/10.1016/j.ijhydene.2022.12.346.

[14] Y.R. Lu, P.A. Nikrityuk, DEM-based model for steam methane reforming, Chemical Engineering Science 247 (2022) 116903, https://doi.org/10.1016/j.ces.2021.116903.

[15] M. Zeppieri, P.L. Villa, N. Verdone, M. Scarsella, P. De Filippis, Kinetic of methane steam reforming reaction over nickel- and rhodium-based catalysts, Applied Catalysis A: General 387 (2010) 147–154, https://doi.org/10.1016/j.apcata.2010.08.017.

[16] J. Xu, G.F. Froment, Methane steam reforming, methanation and water-gas shift: I. Intrinsic kinetics, AIChE journal 35 (1989) 88–96, https://doi.org/10.1002/aic.690350109.

[17] V. Tacchino, P. Costamagna, S. Rosellini, V. Mantelli, A. Servida, Multi-scale model of a top-fired steam methane reforming reactor and validation with industrial experimental data, Chemical Engineering Journal 428 (2022) 131492, https://doi.org/10.1016/j.cej.2021.131492.

[18] P. Virtanen, R. Gommers, T.E. Oliphant, M. Haberland, T. Reddy, D. Cournapeau, E. Burovski, P. Peterson, W. Weckesser, J. Bright, S.J. van der Walt, M. Brett, J. Wilson, K.J. Millman, N. Mayorov, A.R.J. Nelson, E. Jones, R. Kern, E. Larson, C. J. Carey, I. Polat, Y. Feng, E.W. Moore, J. VanderPlas, D. Laxalde, J. Perktold, R. Cimrman, I. Henrik- sen, E.A. Quintero, C.R. Harris, A.M. Archibald, A. H. Ribeiro, F. Pe- dregosa, P. van Mulbregt, SciPy 1.0 contributors, SciPy 1.0: fundamental algorithms for scientific computing in python, Nature Methods 17 (2020) 261–272, https://doi.org/10.1038/s41592-019-0686-2.

[19] A.A. Sheikh, F.R. Bianchi, D. Bove, B. Bosio, A review on MCFC matrix: state-of-the-art, degradation mechanisms and technological improvements, Heliyon 10 (2024) e25847, https://doi.org/10.1016/j.heliyon.2024.e25847.

[20] M. Spinelli, M.C. Romano, S. Consonni, S. Campanari, M. Marchi, G. Cinti, Application of molten carbonate fuel cells in cement plants for CO_2 capture and clean power generation, Energy Procedia 63 (2014) 6517–6526, https://doi.org/10.1016/j.egypro.2014.11.687.

[21] D. Bove, E. Audasso, T. Barckholtz, G. Kiss, J. Rosen, B. Bosio, Process analysis of molten carbonate fuel cells in carbon capture applications, International Journal of Hydrogen Energy 46 (2021) 15032–15045, https://doi.org/10.1016/j.ijhydene.2020.08.020.

[22] D.W. Green, R.H. Perry, Perry's Chemical Engineers' Handbook, Eighth Edition, McGraw-Hill, New York, 2008.

[23] R.B. Bird, W.E. Stewart, E.N. Lightfoot, Transport Phenomena, John Wiley & Sons Inc, 2007.

[24] E.N. Sieder, G.E. Tate, Heat transfer and pressure drop of liquids in tubes, Industrial & Engineering Chemistry 28 (1936) 1429–1435, https://doi.org/10.1021/ie50324a027.